Plasma flows during the ablation stage of an over-massed pulsed-power-driven exploding planar wire array

Citation: R. Datta, J. Angel, J. B. Greenly, S. N. Bland, J. P. Chittenden, E. S. Lavine, W. M. Potter, D. Robinson, T. W. O. Varnish, E. Wong, D. A. Hammer, B. R. Kusse, J. D. Hare; Plasma flows during the ablation stage of an over-massed pulsed-power-driven exploding planar wire array. Phys. Plasmas 1 September 2023; 30 (9): 092104.

As Published: 10.1063/5.0160893

Publisher: AIP Publishing

Persistent URL: https://hdl.handle.net/1721.1/156896

Version: Final published version: final published article, as it appeared in a journal, conference proceedings, or other formally published context

RESEARCH ARTICLE | SEPTEMBER 06 2023

Plasma flows during the ablation stage of an over-massed pulsed-power-driven exploding planar wire array

R. Datta ; J. Angel; J. B. Greenly; S. N. Bland ; J. P. Chittenden ; E. S. Lavine ; W. M. Potter ; D. Robinson; T. W. O. Varnish ; E. Wong ; D. A. Hammer ; B. R. Kusse ; J. D. Hare

Phys. Plasmas 30, 092104 (2023)
https://doi.org/10.1063/5.0160893

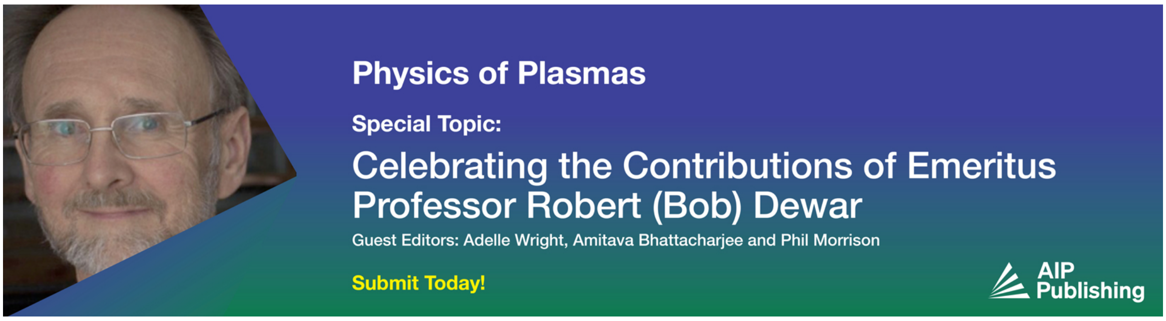

Physics of Plasmas ARTICLE pubs.aip.org/aip/pop

Plasma flows during the ablation stage of an over-massed pulsed-power-driven exploding planar wire array

Cite as: Phys. Plasmas **30**, 092104 (2023); doi: 10.1063/5.0160893
Submitted: 6 June 2023 · Accepted: 17 August 2023 ·
Published Online: 6 September 2023

View Online Export Citation CrossMark

R. Datta,[1] J. Angel,[2] J. B. Greenly,[2] S. N. Bland,[3] J. P. Chittenden,[3] E. S. Lavine,[2] W. M. Potter,[2] D. Robinson,[1] T. W. O. Varnish,[1] E. Wong,[1] D. A. Hammer,[2] B. R. Kusse,[2] and J. D. Hare[1,a)]

AFFILIATIONS

[1]Plasma Science & Fusion Center, Massachusetts Institute of Technology, Cambridge, Massachusetts 02139, USA
[2]Laboratory of Plasma Studies, Cornell University, Ithaca, New York 14853, USA
[3]Blackett Laboratory, Imperial College London, London SW7 2BW, United Kingdom

[a)]Author to whom correspondence should be addressed: jdhare@mit.edu

ABSTRACT

We characterize the plasma flows generated during the ablation stage of an over-massed exploding planar wire array, fielded on the COBRA pulsed-power facility (1 MA peak current, 250 ns rise time). The planar wire array is designed to provide a driving magnetic field (80–100 T) and current per wire distribution (about 60 kA), similar to that in a 10 MA cylindrical exploding wire array fielded on the Z machine. Over-massing the arrays enables continuous plasma ablation over the duration of the experiment without implosion. The requirement to over-mass on the Z machine necessitates wires with diameters of 75–100μm, which are thicker than wires usually fielded on wire array experiments. To test ablation with thicker wires, we perform a parametric study by varying the initial wire diameter between 33 and 100 μm. The largest wire diameter (100 μm) array exhibits early closure of the cathode-wire gap, while the gap remains open over the duration of the experiment for wire diameters between 33 and 75 μm. Laser plasma interferometry and time-gated extreme-ultraviolet (XUV) imaging are used to probe the plasma flows ablating from the wires. The plasma flows from the wires converge to generate a pinch, which appears as a fast-moving ($V \approx 100$ kms^{-1}) column of increased plasma density ($\bar{n}_e \approx 2 \times 10^{18}$cm^{-3}) and strong XUV emission. Finally, we compare the results with three-dimensional resistive-magnetohydrodynamic (MHD) simulations performed using the code GORGON, the results of which reproduce the dynamics of the experiment reasonably well.

I. INTRODUCTION

Inverse (or "exploding") cylindrical wire arrays are a commonly used pulsed-power-driven source of magnetized plasma for laboratory astrophysics applications. These arrays consist of a cylindrical cage of thin conducting wires surrounding a central cathode. This magnetic field configuration drives radially diverging outflows into a vacuum region, providing good diagnostic access.[1] These arrays have previously been fielded on 1 MA university-scale facilities to study a variety of astrophysical phenomena, including magnetized plasma shocks,[2–5] laboratory magnetospheres,[6] and magnetic reconnection.[7,8] For such applications, the wire arrays are typically over-massed, so that they provide continuous sustained plasma flows over the duration of the experiment.[9]

On larger pulsed-power machines, such as the Z machine (30 MA peak current, Sandia National Labs),[10,11] over-massed exploding wire arrays require a larger initial mass due to the higher driving current.[9] For the same wire material, this necessitates more wires and/or the use of larger diameter wires. Although arrays with thin (5–40μm diameter) wires have been characterized extensively in pulsed-power-driven experiments,[9,12,13] there has been little systematic effort to study ablation from thick (>50μm diameter) wires, especially with Z-relevant > 100 T driving magnetic fields.[11]

In cylindrical wire arrays, the maximum driving magnetic pressure is limited by the size of the central cathode and the cathode-wire (CW) gap. The driving magnetic field in a cylindrical array can be determined from Ampère's law: $B(t) = \mu_0 I(t)/(2\pi R)$, which shows that it varies inversely with the radius R of the array.[9] For an $R = 10$mm array, the peak driving field on a typical 1 MA university-scale machine is $B = 20$ T. The finite size of the central cathode makes it difficult to achieve ~100 T driving magnetic fields using cylindrical arrays on 1 MA university-scale facilities. In order to overcome this limitation, we explore the use of planar wire arrays to test ablation from thick wires in Z-relevant driving magnetic fields.

These planar wire arrays consist of a linear arrangement of wires separated by a small CW gap from a planar return electrode. This exploding planar geometry, which has previously been fielded on 1 MA pulsed-power devices,[14] allows us to achieve higher driving magnetic fields than in cylindrical arrays. We also investigate the use of planar wire arrays as a platform for laboratory astrophysics experiments. Since exploding cylindrical arrays generate azimuthally symmetric flows, the majority of the plasma (and therefore the stored energy) is lost in directions that are not of interest.[7,8] Moreover, due to radially diverging flows, the density and advected magnetic field decrease rapidly with distance from the wires.[3,5] In contrast, planar wire arrays could provide directed flows of denser plasma with higher advected magnetic fields, which can be desirable for many laboratory astrophysics applications. In magnetic reconnection experiments, for instance, this would increase dissipation in the current sheet, which is necessary for studying radiative-cooling effects.[15,16]

Planar wire arrays were primarily developed as an efficient x-ray radiation source for indirect-drive inertial confinement fusion (ICF) experiments.[17–21] In contrast to the exploding geometry used in this paper, the wire arrays used for x-ray generation typically consist of a linear row of wires between the cathode and the anode of the pulsed-power device, without the planar return electrode placed adjacent to the wires. Furthermore, these arrays use thin 5–20μm diameter wires, which implode during the course of the experiment.[17,19,20] The arrays are designed such that the implosion time matches the time of the peak current, in order to maximize the x-ray emission (hence, they are also called matched arrays).[20] The implosion stage typically proceeds in a cascade-like fashion, where the imploding wires, starting from the outermost wires, accelerate toward the geometric center of the array to form a strongly radiating inhomogeneous plasma column.[18,20] These array configurations have been reported to exhibit a peak x-ray power and yield higher than imploding cylindrical arrays with similar number of wires.[19,20] Bland *et al.* were the first to field the planar wire array in an exploding geometry. This geometry, which consisted of a matched planar array with thin 7.5μm tungsten wires, exhibited a 5–6$\times$ higher ablation rate compared to cylindrical wire arrays, consistent with the increased driving magnetic pressure inside the CW gap.[14] Furthermore, the ablating plasma converged to form a magnetic precursor column offset from the plane of the wires, before exhibiting the cascade-like implosion.[14]

In contrast to the previous planar wire array experiments described above, which use matched arrays with thin wires, we use over-massed arrays with thick 33–100μm aluminum wires. Using an initial wire mass greater than that of a matched array suppresses the implosion stage and generates continuous plasma ablation over the course of the experiment. In wire arrays, the initial flow of current through the wires forms dense cold wire cores surrounded by low-density coronal plasma.[9,12] Current density is concentrated in a thin skin region on the inner surface of the wires and includes the coronal plasma. Initially, when the driving magnetic field is small, the wire cores expand isotropically at a rate comparable to the local sound speed due to the pressure gradient force. When the global $\mathbf{j} \times \mathbf{B}$ force becomes comparable to the pressure gradient force, it redirects the coronal plasma expanding into the CW gap.[22] In a planar wire array, this generates plasma flows directed away from the CW gap.[14] The ablating plasma advects some magnetic field from the CW gap as it flows outwards, creating outflows of magnetized plasma. In matched arrays, when the stationary wire cores begin to run out of mass (typically ~50%–80% of the initial mass), periodic breaks appear in the wires, driven by the growth of a modified $m = 0$-like axial instability.[9,22–24] This marks the end of the ablation phase and the beginning of the implosion phase.[9]

In arrays with an inter-wire gap-to-core size ratio greater than a critical ratio of π, the wire cores remain unmerged after their thermal expansion.[25] This enables the $\mathbf{j} \times \mathbf{B}$ force to redirect the coronal plasma from the inner surface of the wires (where the current density is concentrated) around the stationary wire cores and into the flow region outside the wires, resulting in the ablation of plasma as individual streams from the wire cores.[25,26] In contrast, when the gap-to-core size ratio is smaller than π, the wire cores merge to generate a plasma shell. The merging of cores is undesirable for sustained ablation because it prevents the movement of coronal plasma and frozen-in magnetic flux from the inner surface of the wires into the flow region.[25] A large core size may also increase the likelihood of the CW gap closure in pulsed-power-driven systems. Closure of the CW gap is undesirable, as it short-circuits the current path, leading to a decreased current flow through the wires and reduced/terminated ablation. Previous experiments aimed at characterizing the wire core size in imploding wire arrays show that the core diameter varies with the wire material and initial wire diameter but is largely independent of the current per wire and the inter-wire separation.[12]

In this paper, we explore the use of an over-massed exploding planar wire array as a platform for laboratory astrophysics experiments and as a scaled experiment to investigate the ablation of thick wires in cylindrical wire arrays driven by Z-relevant driving magnetic fields. The array is driven by the COBRA pulsed-power machine (1 MA peak current, 250 ns rise time)[27] and is designed to exhibit a magnetic driving pressure, current per wire, and inter-wire separation, comparable to that of a 40mm diameter exploding wire array driven by a 10 MA current pulse from the Z machine.[15,16] These experiments, therefore, allow us to investigate wire ablation on smaller 1 MA facilities in loads designed for use on ~10 MA machines. Loads fielded on higher current 10–20 MA machines are expected to generate denser plasma flows with strong radiative cooling, which enables the investigation of fundamental astrophysical phenomena, such as magnetized shocks and magnetic reconnection, in a new radiatively cooled regime. We note that Bland *et al.* also aimed to match the driving magnetic field of a 20 MA, 100 ns rise time current pulse on the Z machine to understand the imploding cylindrical wire array ablation at higher current per wire and driving magnetic fields. In this paper, we target the driving conditions generated when Z operates in a synchronous long-pulse configuration, with a 20 MA peak current (split between two arrays) and a 300 ns rise time.[15,16] As such, we use the long-pulse mode on COBRA, as described in Sec. II. The requirement to over-mass on the Z machine necessitates wires with diameters of 75–100 μm, which are thicker than wires usually fielded on wire-array z-pinch experiments. To investigate ablation with thicker wires, we vary the initial wire diameter between 33 and 100 μm over multiple shots.

The primary contributions of this work are as follows: (1) we demonstrate and characterize plasma ablation from arrays with very

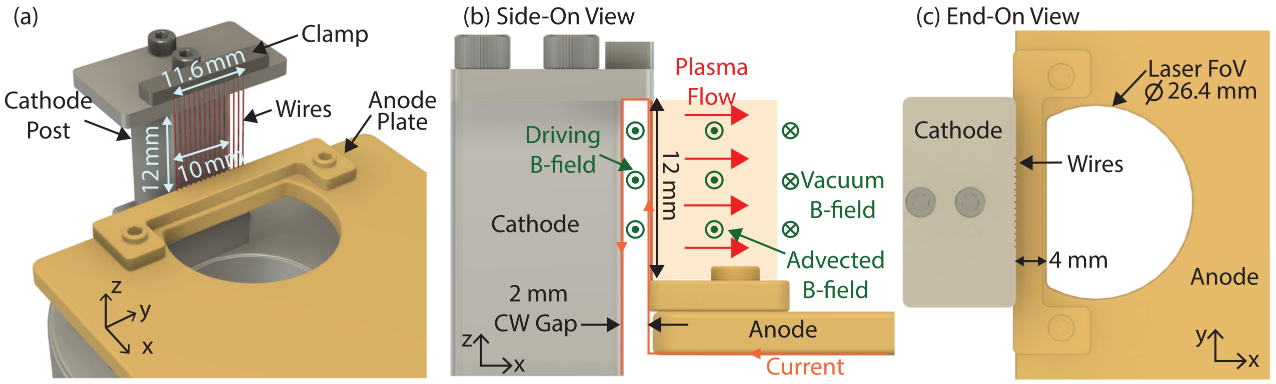

FIG. 1. (a) 3D CAD representation of the load hardware. The load hardware consists of a planar array of 15 equally spaced aluminum wires. (b) Side-on view of the load hardware. The ablated plasma advects the magnetic field from inside the cathode-wire (CW) gap as it flows into the region to the right of the wires. (c) End-on view of the load hardware.

thick 50–100μm wires, not previously fielded on university-scale wire array z-pinches but relevant for laboratory-astrophysics experiments on the Z machine. (2) We characterize the expansion of the wire cores and the surrounding coronal plasma for these thicker wires, the expansion of the cathode plasma, and the development of instabilities at the plasma–vacuum interface in the CW gap. These quantities have not been previously characterized in planar wire arrays and are important for gap closure in pulsed-power-driven experiments. (3) We use overmassed wire arrays, which suppresses the implosion stage and enables us to record the dynamics of the precursor column over a much longer timescale and near peak current. This is in contrast to previous work by Bland *et al.*, where the time between pinch formation and implosion was < 100 ns, which occurred well before the peak current. (4) Our improved interferometry and shadowgraphy diagnostics, compared to previous experiments, also allow us to make quantitative measurements of density and to observe small-scale structures in the plasma along multiple viewing directions. (5) Finally, we augment our experiments by comparing them to the first fully three-dimensional resistive magnetohydrodynamic simulation of an exploding planar wire array implemented with a realistic electrode geometry. These simulations provide a detailed insight into current and force distribution in the load and plasma and describe the formation and ensuing dynamics of the pinch.

II. EXPERIMENTAL AND DIAGNOSTIC SETUP

A. Load hardware

Figure 1 shows the load hardware configuration for this experiment. The load consists of a linear array of 15 equally spaced aluminum wires. The wire-to-wire separation is 0.83mm, and the array height is 12mm. The wires are separated from a 10mm wide stainless-steel cathode by a 2mm wide CW gap and are held in position by clamps on the anode plate and on top of the cathode post. We perform a parametric study by varying the wire diameter between $33 \leq d_{\mathrm{wire}} \leq 100\mu$m for different experimental shots. The COBRA pulsed-power machine (Cornell University),[27] when operated in a long pulse mode, drives a 1 MA peak current pulse through the load.[12,28] A calibrated Rogowski coil placed around the central cathode monitors the current delivered to the load. Figure 2 shows the variation of the current delivered with time, as measured by the Rogowski coil. We show the current pulse averaged over 6 successive shots. The current pulse has a double-peaked structure, as it is formed from staggering the current delivery from two Marx generators by controlling self-breaking switch pressures.[29] The first peak has a magnitude of about 0.75 MA and appears roughly 125 ns after the current start, while the second peak has a magnitude of approximately 1 MA and appears 250 ns after the current start. The shot-to-shot deviation in the current pulse for this experimental series is $<10\%$.

To gain insight into the current distribution and driving magnetic field for the planar wire array, we perform magnetostatic inductance and Biot–Savart calculations of the load hardware.[14] The magnetostatic magnetic field distribution in the planar wire array is shown in Fig. 3(a). The magnetic field inside the CW gap is nearly uniform with y-directed field lines, which curve around the outermost wires to form closed loops outside the array. The mean driving magnetic field (at peak current) inside the CW gap is about 80–100 T. Figure 3(c) shows lineouts of the magnetic field strength along the y-direction inside the CW gap. At the center of the gap ($x = -1$mm), the driving magnetic field is uniform in the middle of the array ($|y| \leq 4$ mm) with a strength of about 81 T but drops sharply to about 50 T near the position of the outermost wires ($y = \pm 6$ mm). This is because in contrast to previous experiments,[14] we use a cathode whose width is smaller than the linear extent of the wires, which decreases

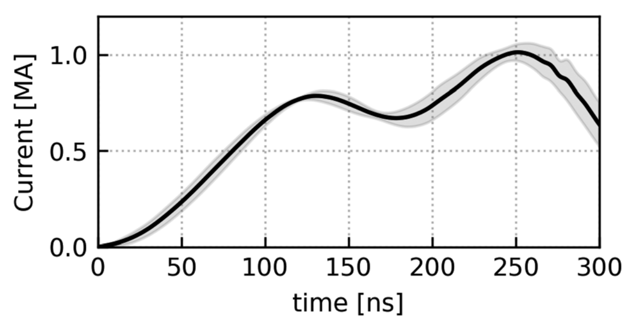

FIG. 2. Variation of the current delivered with time for the COBRA generator. We show the current pulse averaged over six successive shots. The shaded region is the shot-to-shot deviation in the current delivered.

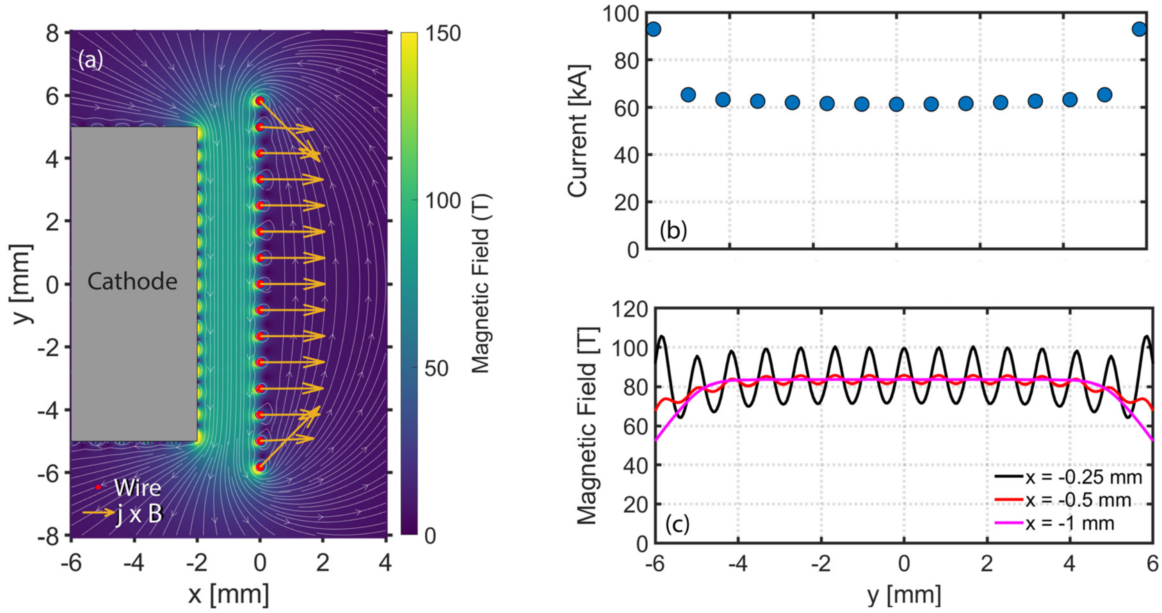

FIG. 3. (a) Simulated magnetostatic magnetic field distribution in the load hardware. (b) Simulated current distribution in the wires at peak current, calculated from a magnetostatic inductance calculation. (c) Variation of the magnetic field strength in the CW gap at a peak current at $x = -0.25, -0.5$, and -1 mm.

the magnetic field strength around the outermost more inductively favorable wires. Closer to the position of the wires, the magnetic field is dominated by the local magnetic field around each wire, resulting in a periodic variation in the field strength, as seen in Fig. 3(c). Finally, unlike cylindrical exploding wire arrays, where field lines form closed loops inside the CW gap and the field decays to zero outside the wires,[2] here, the magnetic field lines must form closed loops outside the CW gap in the planar wire array. This means that there is a non-zero vacuum magnetic field in the flow region to the right of the wires, which is expected to be about 10% of the driving magnetic field from the magnetostatic calculations.

The simulated current distribution in the wires at peak current (1 MA) is shown in Fig. 3(b). The current in the wires is symmetric about the $y = 0$ mm plane and increases slightly with distance from the centerline for the inner wires. The current per wire is about 60–65 kA for the inner wires and increases sharply to approximately 90 kA for the outermost wires. The higher current in the inductively favorable outermost wires has also been reported previously in inductance and wire dynamics model computations of the planar wire array.[14,18] Bland *et al.* considered both the resistive and inductive divisions of current between the wires and found the experimental observations to be more consistent with the inductive current division, driving a much higher current to the outermost wires.[14] Due to the higher current, the rate of mass ablation from the outermost wires is expected to be higher. From a rocket model calculation,[9] assuming 50μm diameter wires, we expect the outermost wires to ablate 50% of their initial mass around 200ns after the current start.

When current flows through the wires, the wires heat up resistively to generate a low-density coronal plasma surrounding the dense wire cores. The global $\mathbf{j} \times \mathbf{B}$ force redirects the coronal plasma expanding into the CW gap, resulting in an outward acceleration of the plasma into the region to the right of the wires.[22] The direction of the vacuum magnetic field in the region to the right of the wires ($x > 0$ mm) can counter-act the outward acceleration of the plasma; however, as shown in Fig. 3(a), the magnetic field in this region is much smaller than the driving field inside the CW gap. Figure 3(a) also shows the direction and the relative magnitude of the $\mathbf{j} \times \mathbf{B}$ force acting on the wire locations. The $\mathbf{j} \times \mathbf{B}$ force at the wires points in the $+x$-direction for the inner wires, and its magnitude remains roughly consistent for the inner wires. The outer wires experience a $\mathbf{j} \times \mathbf{B}$ force directed toward the center of the array. This is due to the bending of the field lines around the outer wires, as observed in Fig. 3(a). In designing the wire array, we explored different cathode sizes and CW gap widths in the magnetostatic simulations; however, the magnetic field always curves around the outer wires, similar to that in previous experiments,[14] leading to an inward-directed $\mathbf{j} \times \mathbf{B}$ force. A shorter cathode relative to the linear extent of the wires, however, allows us to reduce the magnetic field strength around the higher current-carrying outermost wires and, thus, make the magnitude of the $\mathbf{j} \times \mathbf{B}$ force relatively more uniform.

B. Diagnostic setup

We use laser shadowgraphy to visualize the plasma flow from the planar wire array. The shadowgraphy system is set up to provide a side-on view (xz plane) of the experimental setup. This view is shown in Fig. 4(a), which is a pre-shot image of the load. As the laser beam propagates through the plasma, electron density gradients deflect the light away from regions of higher density (lower refractive index) toward regions of lower density (higher refractive index). The intensity measured by the detector is thus related to gradients of electron density.[30]

In addition to shadowgraphy, we use a Mach-Zehnder imaging interferometry system to measure the spatially resolved line-integrated

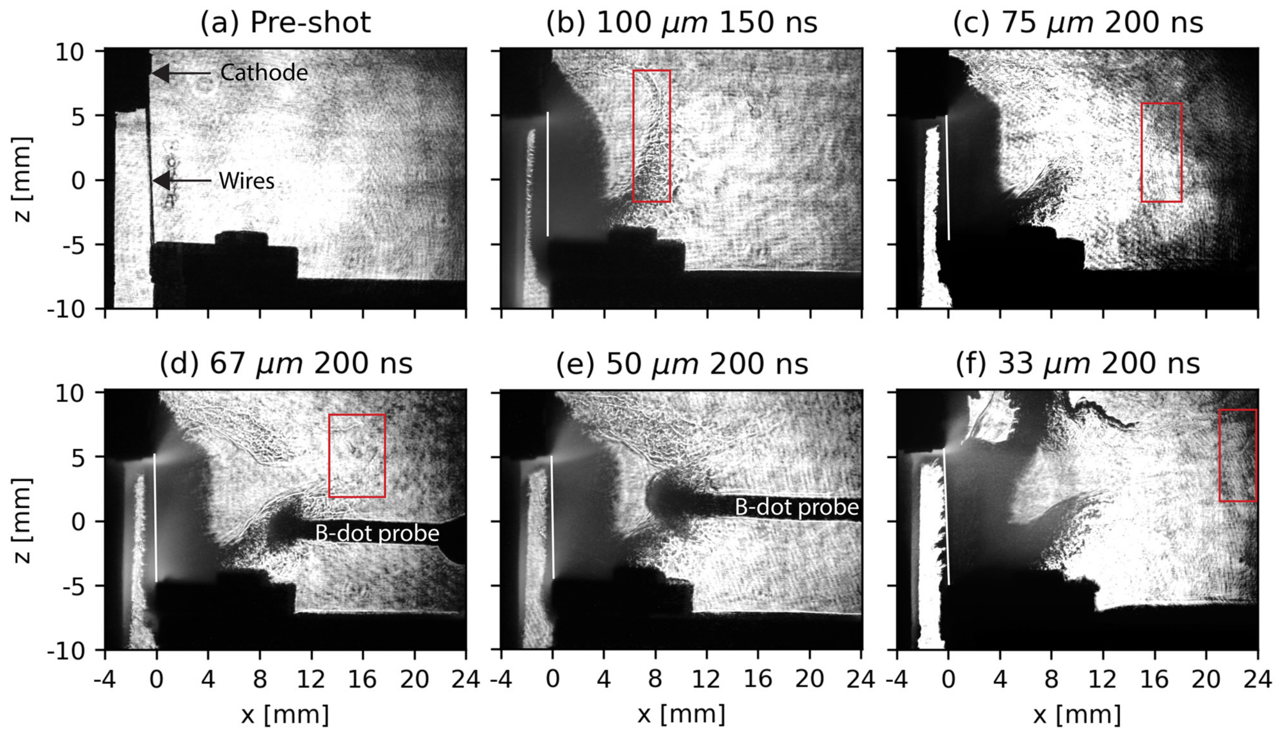

FIG. 4. (a) Shadowgraph of the load hardware recorded before the start of the experiment. (b)–(f) Shadowgraphs of plasma ablation from the planar wire array for different wire diameters $33 \leq d_{\text{wire}} \leq 100\,\mu$m. In each image, the plasma flow is from left to right. We indicate the initial position of the wires, determined from pre-shot images, with a white line. The magnetic precursor column is indicated via a red rectangle. In panels (d) and (e), we also position b-dot probes in the flow.

electron density of the plasma. Our interferometry system is set up to provide both an end-on (*xy* plane) and a side-on view (*xz* plane) of the experimental setup (see Fig. 1). When the probe beam propagates through the plasma, the resulting phase accumulated by the beam distorts the fringe pattern and introduces a spatially varying fringe shift,[31] which we use to reconstruct the phase difference between the probe and reference beams and to determine the spatially resolved line-integrated electron density.[32] The field-of-view of our interferometer includes the volume devoid of plasma, where the fringes remain undistorted. This region of a zero fringe shift is chosen as the region of zero density. Both the shadowgraphy and interferometry systems use a 532nm Nd:YAG laser (150ps pulse width, 100mJ) with a 1 in. diameter field-of-view. In the end-on system, the laser beam enters through a 26.4mm diameter hole in the anode plate, as shown in Fig. 1(c). The interferograms and the shadowgraphs are captured simultaneously using Canon EOS DIGITAL REBEL XS cameras. The interferometry and shadowgraphy systems record 1 frame per shot. The shots are reproducible, and we build up dynamics over multiple shots with identical initial conditions.

We also use a time-gated micro-channel plate (MCP) camera to capture extreme-ultraviolet (XUV) self-emission from the plasma. The camera captures four frames (10 ns inter-frame time, 5 ns exposure time) recorded on isolated quadrants of the MCP via 200μm diameter pinholes. The XUV camera looks onto the wires in the *yz*-plane, with an azimuthal viewing angle of 7.5° with respect to the x axis and a 5° polar angle to the horizontal (*xy*) plane. The diffraction-limited spatial resolution of the system, for photon energies between 10 and 100 eV, is about 180–18 μm, while the geometric resolution is about 300μm.

III. RESULTS

A. Shadowgraphs for different wire diameters

Figure 4 shows the side-on (*xz*-plane) shadowgraphs for different wire diameters $d_{\text{wire}} = 33$–100μm. In each image, plasma flows from the left to the right, and we mark the initial position of the wires, determined from the pre-shot images, using a white line. We record the shadowgraphs at 150 ns after the current start for the 100 μm diameter wire array and at 200 ns for the 33–75μm diameter arrays. In each shadowgraph, the wires expand to form an opaque region around the initial wire position. In this region, the propagating laser beam is lost, either because the density exceeds the critical density of the propagating light ($n_{e,crit} \approx 4 \times 10^{21}\,\text{cm}^{-3}$) or due to strong density gradients, which refract the light out of the optical system's field-of-view. This dense region of plasma expands in the $+x$-direction, driven by the outwardly directed $\mathbf{j} \times \mathbf{B}$ force in the CW gap. Adjacent to the high-density region, we observe a region of relatively uniform density, followed by a narrow column of intensity fluctuations (indicated by a red rectangle in Fig. 4). This plasma column, consistent with the observations of a magnetic precursor column in the literature,[14,20] can be observed further away from the wires for the 33–75μm diameter wires, compared to the 100 μm wire array, which was recorded at an earlier time.

In addition to expansion in the $+x$-direction, the wire cores and the coronal plasma also expand into the CW gap. Figure 5 shows a

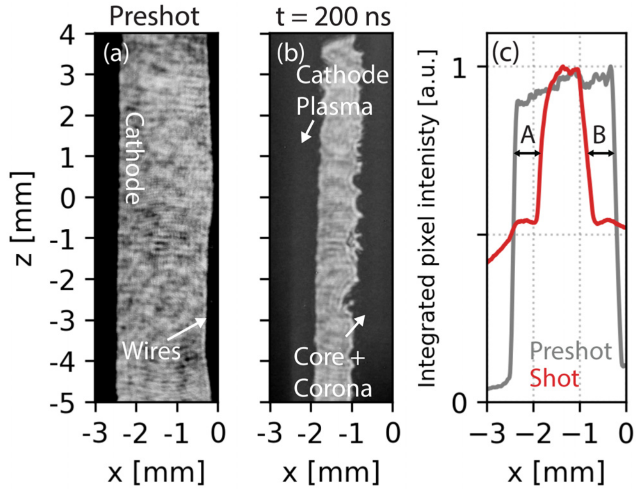

FIG. 5. (a) Pre-shot shadowgraph of the CW gap for 75 μm diameter wires. (b) Expansion of the cathode plasma and the wire core and coronal plasma into the CW gap at 200 ns after the current start. (c) Integrated pixel intensity from shadowgraphy images of the CW gap. The width labeled "A" represents the width of the cathode surface plasma, and "B" is the radius of the expanded coronal plasma.

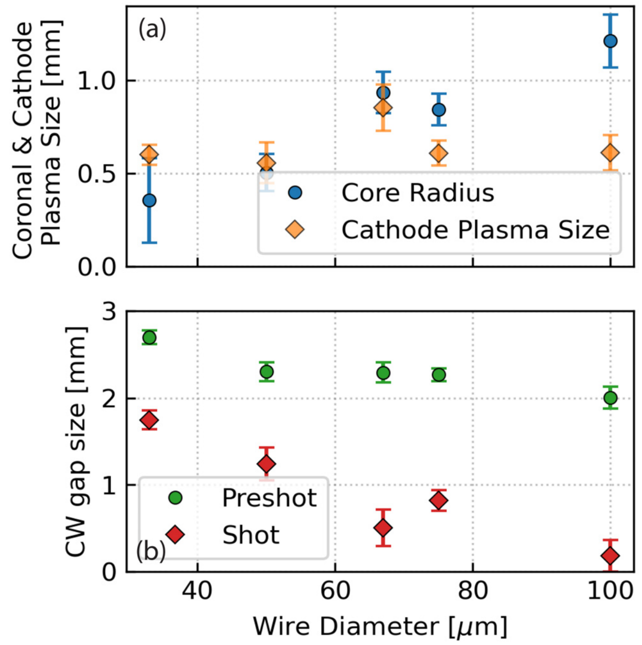

FIG. 6. (a) Variation of the coronal radius and the cathode surface plasma width as a function of the initial wire diameter. (b) Variation of the CW gap size with the initial wire diameter. The range of values shown here comes from the variation in the z-direction.

magnified view of the CW gap for the 75μm wire array, both before the experiment and at 200 ns after the current start. Reduction in the size of the CW gap occurs due to wire core and coronal plasma expansion, as well as the expansion of plasma from the cathode surface. The cathode surface plasma arises from current-driven ablation at the cathode surface and photoionization via soft x-ray radiation generated by the wire cores. As observed in Fig. 4, the array with 100μm wires exhibits the largest reduction in the CW gap size, while the CW gap remains open for wire diameters $d_{\text{wire}} \leq 75\mu$m.

We use the intensity of the shadowgraphs to estimate the diameter of the wire cores and the size of the cathode surface plasma. We crop the shadowgraph to a smaller window, which includes the cathode surface, the CW gap, and the expanding coronal plasma ($-3 \leq x \leq 0$ mm, $|z| \leq 5$ mm) [see Fig. 5(b)] and then integrate the pixel intensity along the z-direction. Figure 5(c) shows the integrated pixel intensity as a function of position x for the 75μm diameter array, both for the pre-shot and for the experimental shadowgraphs. The dark-to-light transitions in the pre-shot intensity profile represent the positions of the cathode surface and the wires, while those in the shot intensity profile represent the "edges" of the cathode plasma and the coronal plasma, respectively. We fit a sigmoid function—the cumulative density of a normal distribution—to the light-to-dark intensity transitions and determine the wire coronal and cathode plasma edges from the means μ of the fitted functions (or equivalently, the full-width-at-half-maximum of the transition). We estimate the uncertainty from the fitted function's standard deviation σ. We can then estimate the width of the cathode plasma from the distance between the cathode plasma edge and the position of the cathode surface [quantity A in Fig. 5(c)]. Similarly, we determine the coronal plasma radius from the distance between the initial wire position and the position of the coronal plasma edge [quantity B in Fig. 5(c)].

Figure 6(a) shows the variation of the coronal plasma radius and the cathode plasma width with varying initial wire diameter. The coronal radius increases with an increasing initial diameter of the wires, while the width of the cathode plasma remains relatively constant at roughly 0.5mm. Figure 6(b) shows the variation of the width of the CW gap with the initial wire diameter. Consistent with the shadowgraphs in Fig. 4, the CW gap width decreases with an increasing wire diameter. The 33μm wires exhibit the smallest reduction in gap size, where the gap decreases from about 2.7mm initially to roughly 1.8mm during the experiment. In contrast, the 100μm wires exhibit the largest decrease in gap size, from about 2mm initially to roughly 0.2mm 150 ns after the current start. The smaller gap size for large wire diameters is primarily due to the increased core and coronal plasma radius of the larger wires. This is in contrast to Bland *et al.*, in which the CW gap closure was almost entirely due to the expansion of plasma from the return electrode and not from the thin 7.5 μm diameter tungsten wires.

The methodology described above provides an upper limit on the wire core diameter. This is because the opaque region in the shadowgraph includes both the wire core and the surrounding coronal plasma. Moreover, density gradients in this region refract the light away from the relatively denser wire cores, resulting in a magnified image. The images could also be dominated by the edge wires, which take more current. Nevertheless, the shadowgraphs reflect the general trend observed in the variation of the core size with wire diameter. X-ray backlighter imaging, which can probe deeper into the core region, can provide a better estimate of the core size. However, this diagnostic was not available for this experimental series. Previous experiments aimed at characterizing the core size report that values determined from shadowgraphs can be 5–10$\times$ larger than that determined from the simultaneous x-ray imaging.[12]

B. Temporal evolution of ablation from the array

We compare side-on shadowgraphs for 50μm diameter wire arrays at 150, 200, and 250 ns in Fig. 7. These shadowgraphs are recorded in separate experimental shots, with identical load hardware. The plasma column (red box in Fig. 7) on the right of the image travels in the $+x$-direction, from $x \approx 12$ mm at 150 ns to $x \approx 22$ mm at 250 ns after the current start. This corresponds to an average velocity of about $100\mathrm{kms}^{-1}$, which is consistent with the magnitude of the flow velocity observed in previous wire array experiments.[6,33] The outward translation of the plasma column in our over-massed array is in contrast to that observed in the under-massed case, where the column remains mostly stationary ($V < 15\mathrm{kms}^{-1}$) between the time of formation and implosion.[14] The reason for this is unclear; however, one hypothesis is that the tungsten plasma used by Bland *et al.* may be colder due to strong radiative emission, and therefore the thermal pressure, that drives the outward motion of the pinch, may be lower and comparable to the restoring force provided by the vacuum field.

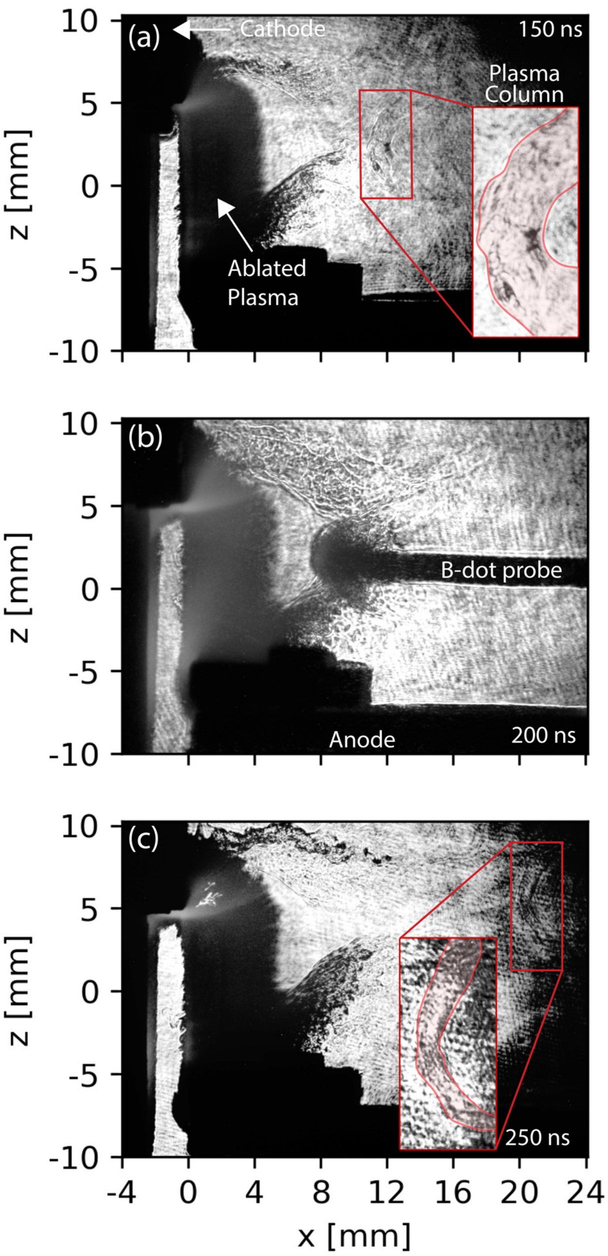

FIG. 7. Plasma ablation from a planar wire array with 50μm diameter wires at (a) 150, (b) 200, and (c) 250 ns after the current start. Shadowgraphs are recorded in separate experimental shots. The red box shows the position of the plasma column, which travels at roughly 100 kms^{-1} between 150 and 250 ns. Note that in panel (b), we have placed a b-dot probe in the flow.

The CW gap remains open throughout the experiment. The temporal evolution of the coronal plasma radius and the cathode plasma width is shown in Fig. 8(a). The measured coronal radius decreases weakly with time, from about 1.2mm at 150 ns to about 0.75mm at 250 ns after the current start. In contrast, the width of the cathode surface plasma remains roughly constant at about 0.5mm. Due to the decreasing coronal plasma radius, the CW gap also becomes slightly larger with time, as observed in Fig. 8(b).

C. Instability growth

Axial perturbations of the coronal plasma appear in the CW gap, as observed in Fig. 5(b). The presence of this axial instability is consistent with previous studies of wire array ablation.[22,34] In Fig. 9, we characterize the amplitude and the wavelength distribution of the instability as a function of the initial wire diameter. We determine the amplitude from half the peak-to-valley distance of the plasma–vacuum interface in the CW gap, which we characterize using the interface-

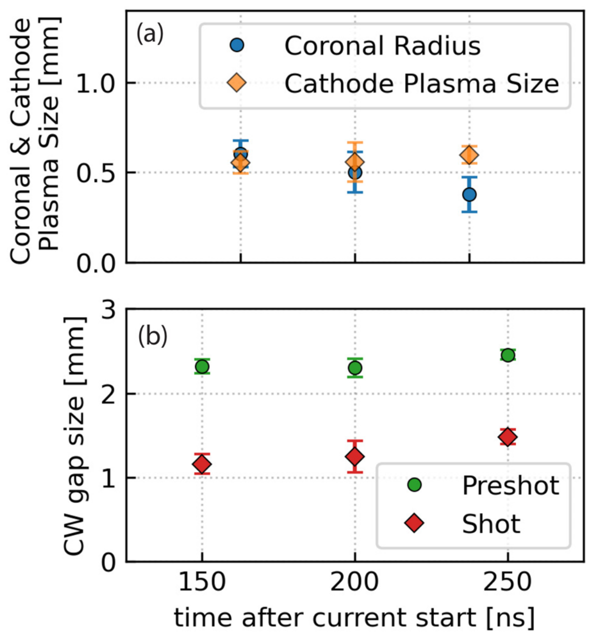

FIG. 8. (a) Temporal variation of the coronal radius and the cathode plasma size for 50 μm diameter wires. (b) Temporal variation of the CW gap for 50 μm diameter wires. Here, each data point comes from a separate experimental shot, and the range of values shown here comes from the variation in the z-direction.

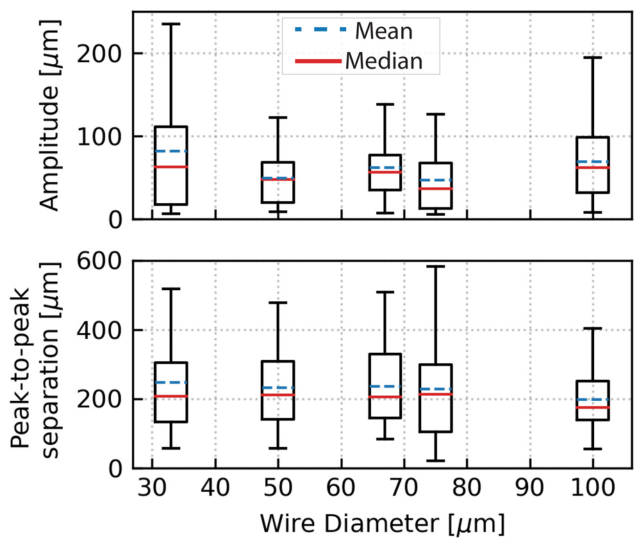

FIG. 9. Variation of the mean amplitude and the peak-to-peak separation of the axial instability in the wire core and the coronal plasma as a function of the initial wire diameter. Values as calculated at 200 ns after the current start for wire diameters 33–75μm and at 150 ns after the current start for the 100μm diameter wires. The red solid line and the blue dashed line represent the median and mean of the distribution, respectively. The bottom and top sides of the rectangle represent the 25th and 75th percentiles, respectively, while the end caps show the full range of the distribution.

detection technique similar to that described in Sec. III A. Similarly, we estimate the wavelength of the instability from the peak-to-peak separation of the perturbations at the plasma–vacuum boundary. In Fig. 9, the red solid line and the blue dashed line represent the median and mean of the distribution, respectively. The bottom and top sides of the rectangle represent the 25th and 75th percentiles (i.e., the interquartile range), respectively, while the end caps show the full range of the distribution. The mean and median values for the perturbation amplitude are similar for most wire diameters and remain largely invariant of the initial wire diameter, with a value of about 50μm. Both the 33 and 100μm wires exhibit a relatively higher upper range of the perturbation amplitude, showing the existence of large amplitude perturbations. The wavelength distribution remains largely independent of the initial wire diameter, with a median peak-to-peak separation of about 200μm. We can also measure the temporal variation of the amplitude and wavelength from the shadowgraphs in Fig. 7. Both the amplitude and wavelength of the instability exhibit little variation with time, which indicates the saturation of the instability growth. We note that the shadowgraphs provide a line-integrated (along the y-direction) view of the perturbation. Therefore, the process of extracting wavelength from the peak-to-peak separation, for the case where peaks from multiple wires overlap along the line-of-sight, becomes more complicated.

D. Electron density measurements

Figures 10(a) and 10(b) show the side-on (xz-plane) interferogram, together with the line-integrated electron density, recorded at $t = 150$ns after the current start for the array with 50 μm diameter wires. We indicate the initial position ($x = 0$ mm) of the wires using a red line. Close to the wires, the high-density plasma forms an opaque region where the probing beam is lost, similar to that in the side-on shadowgraphy images (Fig. 4). Adjacent to this opaque region, where the density is lower, interference between the probe and reference beams forms periodic bright and dark fringes. In this region, the plasma flow from the wires distorts the fringe pattern, whereas, in regions devoid of plasma, the fringes appear undistorted. We trace the fringes by hand and post-process the traced images in MAGIC2 to calculate the line-integrated electron density from the distortion of the fringes.[32] As expected due to time-of-flight effects, the electron density is high close to the wires and decreases with distance from the array. At the plasma–vacuum boundary ($x \approx$ 12–15 mm), the plasma forms a discontinuous column of enhanced electron density. The sharp rise in the electron density in this region indicates the presence of a shock-like structure. The width of the transition is about 2mm. The shape of the plasma column exhibits a significant modulation in the axial direction, consistent with what we observe in the simultaneously recorded shadowgraph of the load [Fig. 7(a)].

Figures 10(c) and 10(d) show the end-on (xy-plane) interferogram and the line-integrated density recorded 150 ns after the current start. The probing laser beam in the region $x < 4$ mm is blocked by the load hardware, but the flow region $x \geq 4$ mm is illuminated via the laser feed shown in Fig. 1(c). As seen in Figs. 10(c) and 10(d), the plasma flow emanating from the wires is redirected toward the center ($y = 0$ mm) of the array. The converging flows collide or "pinch," forming a region of enhanced density, roughly 12–15 mm from the wires. The pinch has also been typically referred to as the "magnetic precursor column" in the wire array literature, as it is the precursor to the final implosion phase, which we suppress in these experiments by over-massing the wire array.[14] The position of the pinch is consistent with that of the column of enhanced electron density observed in the side-on electron density map [Fig. 10(b)].

In Fig. 10(b), at $x \approx 4$ mm from the wires, the line-integrated density is $\langle n_e L_y \rangle \approx$ 5–6 $\times 10^{18}$cm^{-2}, which falls to $\langle n_e L_y \rangle \approx 0.4 \times 10^{18}$cm^{-2} at 11 mm from the wires, right before the position of the pinch. From end-on interferometry [Fig. 10(d)], we estimate the integration length scale L_y by computing the extent of the plasma in the y-direction. This gives us values of $L_y(x = 4\,\text{mm}) \approx 8$ mm and $L_y(x = 11\,\text{mm}) \approx 4$mm. The average electron densities, inferred from $\langle n_e L_y \rangle / L_y$, are therefore $\bar{n}_e \approx 4 \times 10^{18}$cm^{-3} at $x = 4$mm and $\bar{n}_e \approx 1 \times 10^{18}$cm^{-3} at $x = 11$mm from the wires. In Fig. 10(b), the pinch exhibits a line-integrated density of $\langle n_e L_y \rangle \approx 0.8 \times 10^{18}$cm^{-2} at approximately 13 mm from the wires. Assuming a length scale $L_y \approx 4$ mm, the average electron density in the pinch is $\bar{n}_e \approx 2 \times 10^{18}$cm^{-3}. This represents a roughly 2$\times$ jump in the electron density at the pinch compared to the flow upstream of the pinch.

E. XUV self-emission

XUV self-emission images from the load hardware with the 50μm diameter wires are shown in Fig. 11. The wires and the cathode appear as regions of bright emission. Emission from the inner wires appears uniform in intensity, indicating a roughly equal current distribution in the wires, as predicted by the magnetostatic calculation (Fig. 3). The outer wires, however, appear dimmer, which may indicate that the current has switched to the inner wires due to the higher initial rate of ablation from the outer wires, as indicated by the rocket

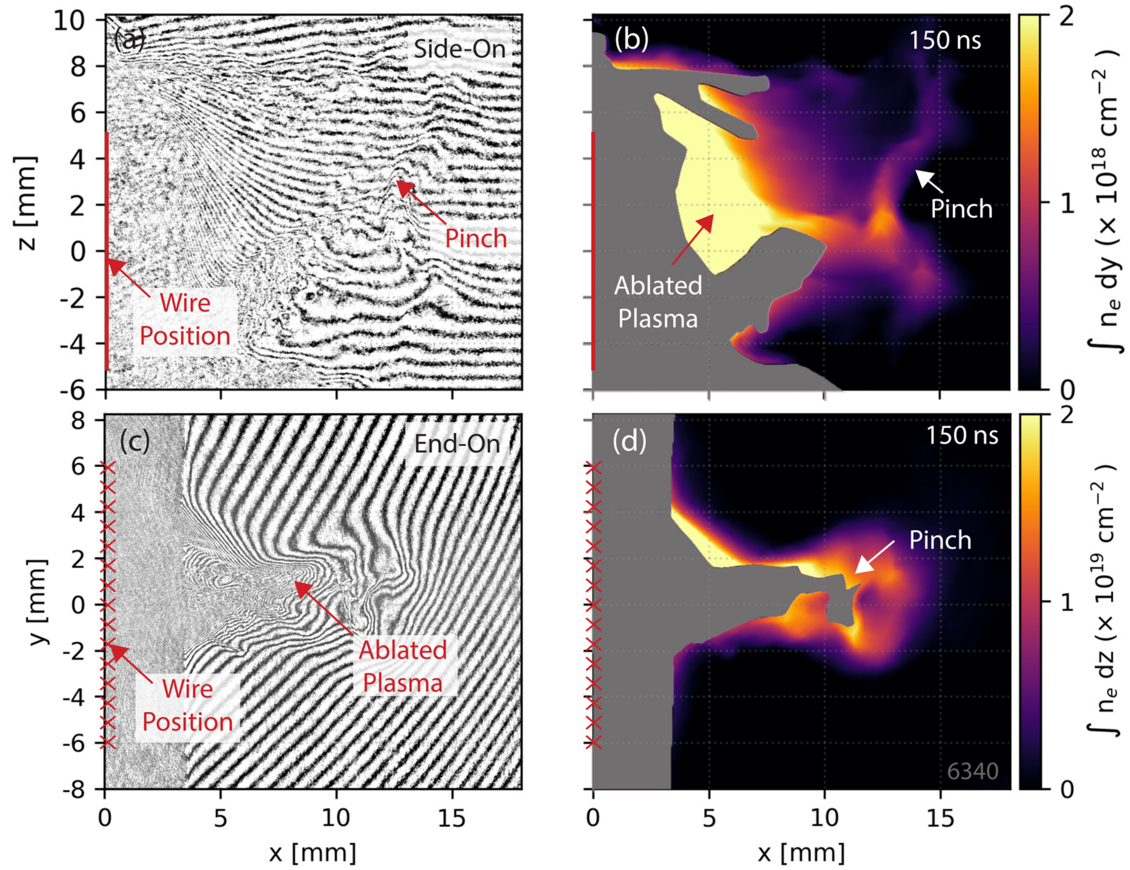

FIG. 10. (a) Side-on raw interferogram for the 50 μm diameter wire array at 150 ns, using a Mach–Zehnder interferometer with a 532 nm laser. (b) Side-on line-integrated electron density map determined from interferometry. (c) End-on raw interferogram at 150 ns after the current start for the 50 μm diameter wire array, recorded during the same experimental shot. (d) End-on line-integrated electron density map determined from interferometry. Regions in gray near the wires represent locations where the probing beam is lost.

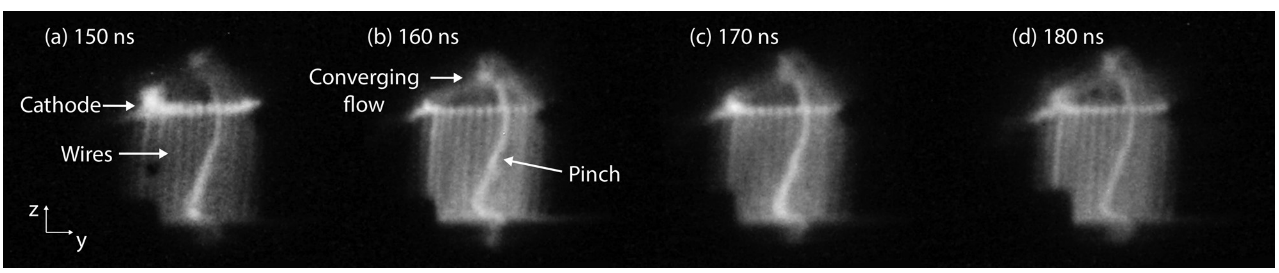

FIG. 11. XUV self-emission images of a planar wire array with 50μm diameter wires. The pinch appears as a column of bright emission.

model calculation in Sec. II A and also observed via x-ray streak imaging in previous experiments.[35,36] Although the wires appear as well-separated columns of emission, the resolution of the optical system prevents us from making quantitative measurements of the core diameter from the XUV images. We observe that the flows from the wires converge to form the pinch, which appears as a brightly glowing column oriented in the z-direction. The increased emission from the pinch is consistent with its higher electron density (Fig. 10). Furthermore, shock heating and Ohmic dissipation in the pinch may also contribute to a higher temperature and, consequently, higher radiative emission. The XUV images also exhibit the axial non-uniformity in the shape of the pinch, consistent with the interferometry and shadowgraphy results [Figs. 7(a) and 10(b)]. We note that the curved shape of the pinch is visible in these images because the XUV camera has a small azimuthal viewing angle of 7.5°, and it does not look normal to the yz-plane. Finally, the structure of the plasma ablation and the pinch remains roughly invariant across the different frames over the observation window of 150–185ns. This is in contrast to the shadowgraphy and interferometry images (Figs. 7 and 10), which show a significant ($V \approx 100 \mathrm{kms}^{-1}$) motion of the pinch. This may indicate that this is a "ghost" image of the pinch recorded when the MCP is not triggered due to a radiation bleed-through at the time when emission from the pinch is at a maximum.

In Fig. 12, we compare the XUV emission from the planar wire arrays with 50 and 100μm diameter wires, respectively. In both cases, the pinch is visible as a bright column of emission, and the shape of the pinch is similar between the two images. For the 50μm diameter case, the wires appear as discrete columns of enhanced emission, as can be observed in lineouts of the intensity at $z = 4$ mm [Fig. 12(c)]. In contrast, the wires are not easily distinguishable for the thicker 100μm, consistent with the core size becoming comparable to the inter-wire separation, as seen in Fig. 6.

IV. DISCUSSION OF RESULTS

A. CW gap and wire core size

Previous wire array experiments with $\sim$10μm diameter wires show that the diameters of the wire cores and the surrounding corona both increase with the initial wire diameter and are largely independent of the current per wire and the inter-wire separation.[12] Our experimental results are consistent with this effect—Fig. 6(a) exhibits a roughly linear increase in the coronal radius with increasing wire diameter, and the measured coronal diameter is roughly 20–25$\times$ the initial wire diameter. While the coronal radius increases with the initial wire diameter, the size of the cathode plasma remains relatively constant [see Fig. 6(a)].

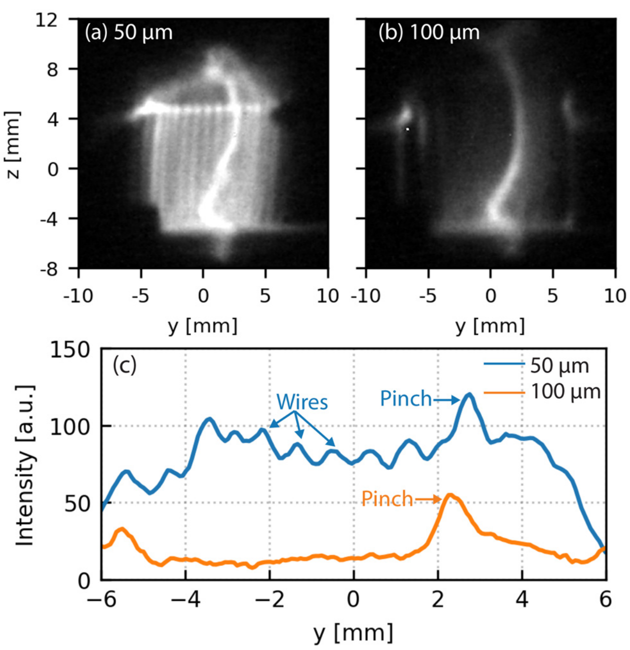

FIG. 12. XUV self-emission images of a planar wire array with (a) 50μm diameter wires and (b) 100μm diameter wires. Wires are easily distinguishable in the 50μm case but not for the 100μm diameter wires. (c) Lineouts of intensity along $z = 4$ mm for 50 and 100μm diameter wires.

This is expected since changing the initial wire diameter is not likely to affect the current distribution through the cathode. The larger coronal radius is, therefore, the primary reason for gap closure in the thick 100μm case. The gap closes at 150 ns after the current start, which makes $d_{\mathrm{wire}} = 100\mu$m an undesirable wire diameter, both in these planar wire experiments and on the Z experiments for which these experiments are a scaled test. Furthermore, the coronal radius also becomes larger than the inter-wire separation in this case, which inhibits plasma ablation and magnetic field advection from the array.[25]

The early gap closure for the 100μm diameter case could be a consequence of the lower Ohmic heating in the skin region around the wire core. The initial electrical explosion of the wires forms a dense cold wire core consisting of vapor and microscopic liquid metal droplets. Without further Ohmic heating by the current, we would expect the wire core radius $R(t)$ to expand isotropically at a rate comparable to its local sound speed C_{core} into the vacuum, i.e., $dR/dt \sim C_{\mathrm{core}}$. For thin wires, the current flowing over the wire core surface in the skin region Ohmically heats the material at the edge of the core, forming coronal plasma that is redirected by the global $\mathbf{j} \times \mathbf{B}$ force. However, if the wire core is sufficiently large, the current density in the skin region $j_{\mathrm{skin}} = I(t)/(2\pi R(t)\delta)$ will be lower. Here, $I(t)$ is the driving current, and $\delta = \sqrt{2\eta/\omega\mu}$ is the resistive skin depth, which depends on the material resistivity η, the angular frequency ω of the driving current, and the medium permeability μ. Consequently, for a large initial wire diameter, the Ohmic heating rate ηj_{skin}^2 may be too small to ionize all of the expanding gas. This will allow the neutral gas expanding out of the wire core to remain un-ionized and, thus, unaffected by the $\mathbf{j} \times \mathbf{B}$ force expelling it from the CW gap. It is this neutral gas that may be responsible for the observed gap closure. In future experiments, the importance of the neutral gas expansion could be tested by exploiting the different refractive indices of plasma and neutral gas using two-color optical measurements.[37]

For the 50 μm diameter wire array, the CW remains open late in time ($t = 250$ ns), and the coronal radius does not exceed the inter-wire separation, which is desirable for good ablation from the array (Fig. 8). In imploding wire arrays, the coronal radius increases initially in time and then saturates to a constant value.[12] The time of saturation, typically 80–100 ns after the current start, corresponds to a change in the magnetic field topology around the wires when the driving global $\mathbf{j} \times \mathbf{B}$ force becomes strong enough to overcome the expansion of the coronal plasma and redirects it to generate ablation streams.[12] In our experiments, we image the wires after the expected time of saturation and, therefore, do not expect a significant temporal variation in the size of the wire cores between 150 and 250 ns after the current start. As observed in Fig. 8(a), the coronal plasma radius decreases weakly with time at a rate of about $2\mu \mathrm{mns}^{-1}$ for 50 μm diameter wires.

The axial instability of the wires is ubiquitous in wire array z-pinch experiments and is thought to be a modified $m = 0$-like instability, which exhibits a constant amplitude and wavelength later in time and is largely independent of the initial wire diameter and current per wire.[9,22,23] The time of saturation of the instability also corresponds to the time at which the wire cores cease to grow.[22,23] In Fig. 9, we observe that the distributions of the amplitude and the peak-to-peak separation of the perturbations remain largely independent of the initial wire diameter, consistent with observations of the axial instability in imploding wire array z-pinches. The amplitude and the peak-to-peak separation also exhibit minimal variation in time between 150 and 250 ns, which is well after the expected time of saturation of the instability (~80–100 ns).[12,23]

B. Pinch formation and comparison with 3D resistive MHD simulations

To obtain greater insight into the ablation process, we perform three-dimensional simulations of the planar wire array using GORGON, a 3D (cartesian, cylindrical, or polar coordinate) Eulerian resistive MHD code with van Leer advection, and separate energy equations for ions and electrons.[22,38] We use an optically thin recombination-bremsstrahlung radiation loss model, modified with a constant multiplier to account for line radiation, and a Thomas–Fermi equation-of-state to determine the ionization level.[38] We simulate a planar wire array with the same geometric dimensions and wire material as in the experimental setup. The current pulse applied to the load was determined from a three-term sum-of-sines fit $[\sum_i a_i \sin(b_i t + c_i)]$ to the integrated Rogowski signal shown in Fig. 2. The simulation domain is a cuboid with dimensions $51.2 \times 50.4 \times 38$ mm^3. We use an initial wire diameter of 50μm in the simulation, with the initial mass of the wire distributed over a 400μm diameter circular pre-expanded wire core. The simulations are performed with a grid size of 50μm. The driving magnetic field, calculated from Ampère's law, is applied as a boundary condition at the bottom-most cells in the simulation domain between the anode and the cathode of a coaxial transmission line. The load geometry is implemented as a stationary realistic conductivity electrode material on top of the coaxial line.

Figures 13(a) and 13(b) show the simulated current density distribution at a slice in the xy-plane at 70 ns (before pinch formation) and at 200 ns (after pinch formation), respectively. As expected, due to the skin effect, the current density is concentrated on the outer surfaces of the cathode and the wires. The plasma from the outermost wires carries significantly more current than that from the inner wires, consistent with our magnetostatic prediction (Fig. 3). Similar to the experiment, the converging plasma flows collide at $y = 0$mm midplane to form the pinch. The pinch appears as a region of high current density, comparable to that in the wires. Figure 14(a) shows a three-dimensional rendering of the current distribution in the load at $t = 150$ns. The pinch carries a significant amount of current and provides a secondary path for the current to close between the anode and the cathode. In our simulation, the current in the pinch, determined from the area integral of the current in the dashed box shown in Fig. 13(b), is roughly 30% of that in the wires. This is consistent with the estimate of 30%–40% provided by Bland *et al.*[14]

Figures 13(a) and 13(b) also show the distribution of magnetic field lines in the planar wire array. We determine the field lines from streamlines of the magnetic field. Near the CW gap, the magnetic field topology is similar to that calculated from our magnetostatic simulation (see Fig. 3). The magnetic field lines are straight and uniform inside the CW gap and bend around the outer wires to form closed field lines outside the array. The ablating plasma advects some of the magnetic field from inside the array to the outside. Near the inner wires, the advected magnetic field lines are straight and uniform, oriented along the y-direction. However, away from the centerline ($y = 0$mm) and toward the edges of the plasma flow, the field lines bend, driven by the inward-directed ablation from the outermost wires. The spatial variation of the driving magnetic field along the z-direction inside the CW gap is small (<5%).

The arrows in Figs. 13(a) and 13(b) show the direction of the $\mathbf{j} \times \mathbf{B}$ force acting on the ablated plasma. Near the inner wires, where the magnetic field is oriented in the y-direction, the force is directed in the $+x$-direction, whereas at the outermost wires, the curvature of the magnetic field results in a force directed toward the center of the array. As the plasma propagates away from the wires, the bending of the field lines due to the flows from the outermost wires results in an inward-directed (along the y-direction) $\mathbf{j} \times \mathbf{B}$ force. This drives the collision of the plasma flows emanating from the wires and the formation of the pinch. The magnetic field lines around the pinch are three-dimensional and do not close in the same xy-plane in which they originate. Figure 13(c) shows a contour map of current density in the pinch, together with the local 3D magnetic field line topology. The magnetic field lines wrap around the pinch, and the $\mathbf{j} \times \mathbf{B}$ force is directed toward the center of the pinch, similar to a classical z-pinch. However, unlike a classical z-pinch, the pinch experiences both mass and momentum injection from the left side of the pinch. Driven by the magnetic and thermal pressure of the plasma behind the pinch, the pinch accelerates in the $+x$-direction. In the simulation, the center of the pinch travels about 8mm between 150 and 250 ns, resulting in

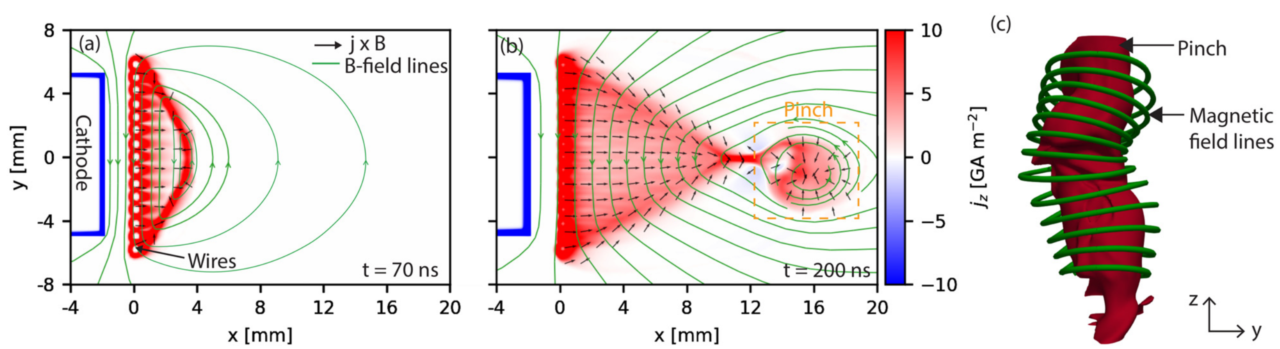

FIG. 13. Current distribution in the load hardware from 3D resistive MHD simulations of the experiment at (a) 70 ns after the current start (before pinch formation) and (b) 200 ns. Here, we show the current distribution on an xy-slice through the load geometry. The black arrows represent the direction of the $\mathbf{j} \times \mathbf{B}$ force, while the green lines are streamlines of the magnetic field. Magnetic field lines around the pinch do not close in this plane because they are three-dimensional in nature. (c) Three-dimensional current density contour map of the pinch and its associated magnetic field topology.

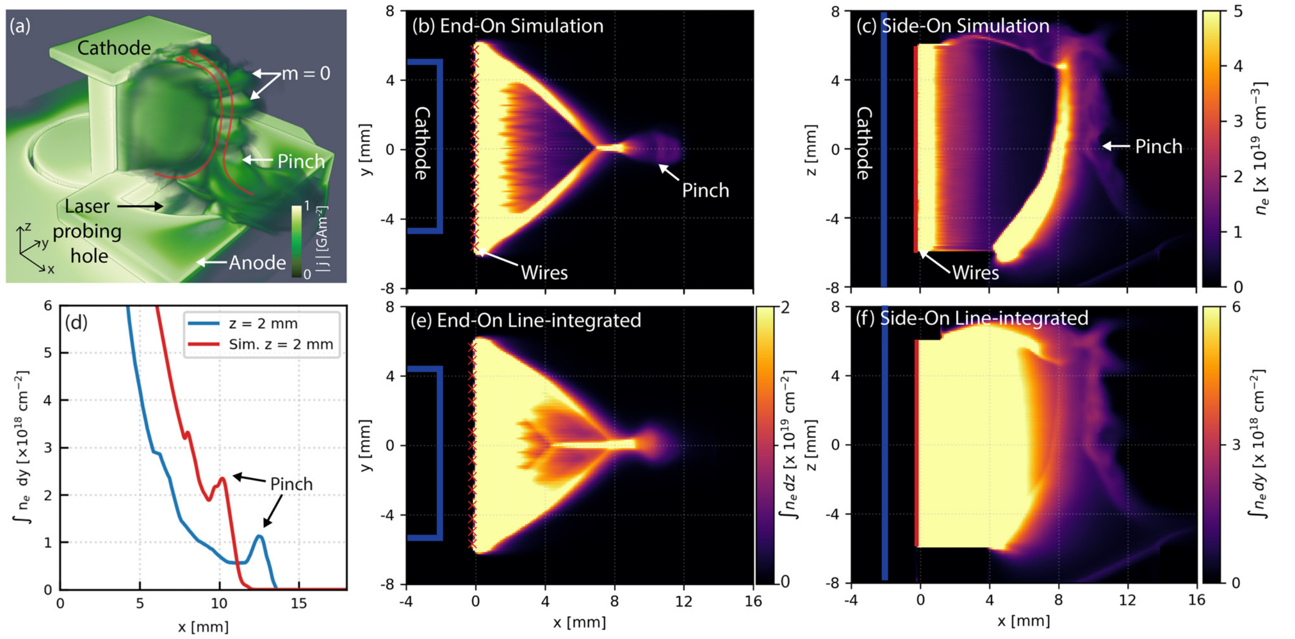

FIG. 14. (a) Simulated current distribution in the load hardware at 150 ns after the current start. The red arrows show the current path. (b) End-on (*xy*-plane) slice of the simulated electron density at the array midplane at 150 ns. (c) Side-on (*xz*-plane) slice of the simulated electron density at the array midplane at 150 ns. (d) Comparison of the line-integrated (along *y*) electron density between the experiment and the simulation. (e) End-on line-integrated electron density. (f) Side-on-line-integrated electron density. Plasma flow is from left to right. Wire positions are indicated by X's in panels (b) and (e) and by red lines in panels (c) and (f). The simulation shows converging flows and the formation of a pinch roughly 8 mm from the wires.

an average velocity of 80kms^{-1}. This is about 20% lower than that inferred from the translation of the pinch in the experimental shadowgraphs (Fig. 7). The flow upstream of the pinch is both supersonic ($M_S \approx 6$) and super-Alfvénic ($M_A \approx 2$), similar to that observed in previous pulsed-power-driven experiments of aluminum wire arrays.[3–5] Due to the high current density in the pinch, it is a site of strong Ohmic dissipation. The electron temperature inside the pinch is $T_e \approx 100$ eV, which is significantly higher than that in the plasma flow behind the pinch $T_e \approx 6.5$ eV. The temperature of the plasma near the wires is also about 5 eV, which may explain why the wires appear dimmer in the XUV images compared to the pinch (Fig. 11). The plasma generated by the wire array is highly collisional with an ion–ion mean free path of about 1×10^{-6}cm. This value of the mean free path is calculated using the characteristic values of electron density $n_e = 1 \times 10^{18}$cm^{-3} and temperature $T_e = 5$ eV. As discussed before, the temperature inside the pinch is higher; however, the plasma still remains highly collisional, with an ion–ion mean free path ($\lambda_{ii} \approx 1 \times 10^{-5}$cm) much smaller than the size of the pinch.

We also observe regions of negative current density on either side of the neck region just upstream of the pinch in Fig. 13(b). We interpret this negative current to be caused by the inverse skin effect, which drives reverse currents on the surfaces of conductors when the driving current decreases in time.[39] An alternative and equivalent way of thinking of this is in terms of the distortion of magnetic field lines as the current carrying plasma column moves. As observed in Fig. 13(b), the field lines around the pinch are distorted along the *x*-direction as the pinch moves from left to right, dragging with it the magnetic field ($R_m \approx 20$–40). From Ampère's law $\nabla \times \mathbf{B} = \mu_0 \mathbf{j}$, the change in B_y along the *x*-direction drives the negative current, identical to the result obtained by interpreting this negative current as due to the inverse skin effect.

Figure 14(b) shows a slice of the simulated electron density at the array midplane ($z = 0$mm) at 150 ns after the current start. The electron density distribution appears similar to that in the experiment (Fig. 10). The electron density is highly closer to the wires and falls with increasing distance in the *x*-direction, consistent with time-of-flight effects. The plasma flow from the inner wires is directed outwards along the *x*-direction, while that from the outermost wires is directed toward the center of the array. The flow converges, similar to that in the experiment, to form a pinch. Figure 14(c) shows a side-on slice of the electron density through the array midplane ($y = 0$mm). The pinch appears as a discontinuous region of enhanced electron density at the vacuum-plasma boundary, similar to that in the experiment. Immediately behind the pinch, both the end-on and side-on slices show a region of lower density, consistent with the relatively uniform intensity region observed in the experimental shadowgraphs (Fig. 7). The electron density inside the pinch is $n_e \approx 4 \times 10^{19}$cm^{-3}, while that in the plasma flow just behind the pinch is 2×10^{18}cm^{-3}. Our experimentally inferred value of the density behind the pinch is consistent with the simulation, while that for the pinch is lower than the density observed in the simulation. This may indicate that the integration length scale used to determine the experimental estimate of density is an overestimation of the true value. As observed in Fig. 14(a), the width of the simulated pinch is approximately 1.5mm, whereas we estimate a value of about 4mm from our experimental end-on density map [Fig. 10(d)]. This discrepancy can result from line integrating through the axially modulated pinch, which widens the observed width of the pinch in the line-integrated density map (Fig. 10). Using an integration length of 1.5 mm results in an electron density of $\overline{n}_e \approx 5 \times 10^{18}\text{cm}^{-3}$, which is closer to, although still lower than, the density of the pinch in the simulation.

Figures 14(e) and 14(f) show the line-integrated electron density in the end-on (xy-plane) and side-on (xz-plane) planes, respectively. In Fig. 14(d), we compare lineouts of the simulated electron density integrated along the y-direction with that from the experiment at $z = 2$mm. In both the experiment and the simulation, the line-integrated density falls with the distance from the wires, and the pinch appears as a local enhancement of the density at the plasma-vacuum boundary. The magnitude of the line-integrated electron density in the simulation is comparable to that from the experiment. Note that the sharp increase in density at the pinch, as observed in Fig. 14(c), is muted by line integration. The high density and the temperature of the pinch both contribute to the strong emission from the pinch, visible in the experimental XUV self-emission images (Fig. 11).

In contrast to the experiment, where the pinch is located at $x \approx 12$–15 mm from the wires, the simulated pinch is closer to the wires ($x \approx 10$ mm) at this time. The slower velocity of the pinch in the simulation indicates a comparatively smaller driving force behind the pinch. We expect the pinch to be driven outwards due to the magnetic and thermal pressures of the plasma behind it. A simple similarity argument can be used to show that the characteristic velocity of the pinch should be comparable to the local magnetosonic velocity $V_{pinch}^2 \sim (V_A^2 + C_S^2)$. Here, V_A is the Alfvén speed, and C_S is the sound speed of the plasma right behind the pinch. A previous comparison of experimental results with simulations indicates that the local thermodynamic equilibrium Thomas–Fermi model implemented in the simulation underestimates the temperature of the plasma.[3] The Alfvén speed $V_A = B/\sqrt{\mu_0 \rho}$ is a function of the magnetic field, which, in turn, depends on the magnetic Reynolds number $R_m = UL/\overline{\eta}$. Here, U and L are the characteristic velocity and length scales of the plasma, respectively, ρ is the mass density, and $\overline{\eta} \sim \overline{Z} T_e^{-3/2}$ is the magnetic diffusivity, which varies with the electron temperature T_e and the average ionization $\overline{Z}$ of the plasma. A lower temperature leads to a lower R_m and thus a relatively smaller advected field. This can reduce the magnetic pressure behind the pinch and therefore contribute to a smaller velocity. In future experiments, the optical Thompson scattering could be used to simultaneously characterize the velocity and temperature of the plasma.[40] In our simulation, we find that the magnetic Reynolds number (computed with a length scale L = 1 cm) in the flow to the right of wires varies between $15 < R_m < 30$. This value is comparable to that observed in previous cylindrical wire array experiments, where B-dot probe and Faraday polarimetry measurements have shown the magnetic Reynolds number to be large enough to advect the magnetic field from the CW gap into the flow.[2,3,5,6]

In both the experiment and the simulation, the shape of the pinch exhibits a strong axial non-uniformity, as observed in Figs. 10(b) and 14(c). MHD instabilities are a potential candidate for the modulation in the pinch shape. Our simulation shows evidence for both the $m = 0$ sausage MHD instability, which modulates the pinch diameter [see Fig. 14(a)], and the $m = 1$ instability, which drives the kinking of the pinch [see Fig. 13(c)]. The Alfvén crossing time, which is the characteristic timescale at which we expect MHD instabilities to grow, is roughly 10–20 ns, which is shorter than the experimental timescale. However, the amplitude of the kinking mode observed in our simulation (<1mm) is not large enough to explain the curvature of the pinch in the xz-plane.

Our simulations indicate that the shape of the pinch is, instead, closely related to the path through the plasma over which the current closes between the cathode and the extended anode plate. The simulations were performed for three cases—(a) with the realistic anode geometry comprising an extended anode plate with a hole for laser probing [see Fig. 14(a)], (b) an extended anode plate without a hole, and finally, (c) without an extended anode plate. The strongest curvature was observed in case (a) with the realistic anode geometry. Two parallel current paths, originating from either side of the hole in the anode plate, are indicated in Fig. 14(a) and contribute directly to the shape of the pinch. The current closes between the near end of the hole ($x = 4$mm) and the cathode via the neck region just upstream of the pinch, as well as through the pinch, which connects the far end of the hole to the cathode. In contrast, for the other two cases, where the current path remains uninterrupted by the hole, the pinch appears comparatively straighter. In future experiments, we can mitigate this effect by exploring planar array geometries that do not require the extended anode plate.

V. CONCLUSIONS

In this paper, we explore the use of an over-massed planar wire array as a platform for laboratory astrophysics experiments and as a scaled experiment to investigate the ablation of thick wires in cylindrical wire arrays driven by 10 MA current pulses. We characterize the ablation of plasma from a planar wire array fielded on the COBRA pulsed-power machine (1 MA, 250 ns rise time). The wire array comprises a linear arrangement of 15 equally spaced aluminum wires separated from a planar cathode surface by a 2 mm CW gap. The planar wire array is designed to provide a driving magnetic field (80–100 T) and current per wire distribution (about 60–65 kA), similar to that in an ∼10 MA cylindrical exploding wire array fielded on the Z pulsed-power machine. Magnetostatic calculations show that the driving magnetic pressure inside the CW gap at a peak current (1 MA) is about 81 T, which is higher than that in a typical cylindrical wire array fielded on 1 MA university scale facilities (about 20–40 T). In contrast to the previous planar wire array experiments, the wire arrays are over-massed so that they provide continuous ablation for the duration of the experiment without experiencing the implosion stage.

We perform a parametric study by varying the initial wire diameter between 33 and 100 μm. Laser shadowgraphy images show that the largest wire diameter (100 μm) exhibits an early closure of the CW gap (150 ns after current start), while the gap remains open during the duration of the experiment for wire diameters between 33 and 75 μm. The early closure of the CW gap for the 100 μm diameter case is primarily due to the larger coronal radius of the wires, which may be a consequence of the reduced Ohmic heating in the skin region surrounding the wire cores. For these large diameter wires, the coronal radius also becomes comparable to the CW gap size and the inter-wire separation, which is undesirable for good ablation from the wire array. Axial instabilities appear in the vacuum–plasma interface in the CW gap. The distributions of the amplitude and peak-to-peak separation of the perturbations remain largely invariant of the initial wire diameter, as has been previously observed on imploding and exploding cylindrical wire arrays.

Laser interferometry and time-gated XUV imaging are used to probe the plasma flows. Plasma ablating from the wires is redirected toward the array midplane ($y = 0$ mm), and the resulting collision of the converging flows generates a pinch, which propagates away from the wires at an average velocity of about 100kms^{-1}. The pinch appears as a discontinuous column of enhanced plasma density ($\overline{n}_e \approx 2 \times 10^{18}$cm^{-3}) and strong XUV emission. Three-dimensional resistive MHD simulations reproduce the primary characteristics of the ablation observed from the experiments. Visualization of the current density and magnetic field in the load demonstrates that flows converge under the action of a pinching $\mathbf{j} \times \mathbf{B}$ force. This arises from the bending of magnetic field lines due to the inward-directed flows from the outermost wires. The pinch is a site of high current density and exhibits a magnetic field topology similar to that of a z-pinch. The simulated pinch also exhibits a significantly higher temperature, compared to the plasma behind it, which combined with the enhanced density accounts for the strong XUV emission observed in the experiment.

In summary, our work advances the understanding of plasma ablation from arrays of thicker wires, expands the knowledge of wire core expansion and coronal plasma behavior, investigates the instabilities at the plasma–vacuum interface, examines the dynamics of the precursor column formation and evolution, refines the diagnostic capabilities, and presents a detailed 3D resistive MHD simulation of the experiment, thus providing confidence that arrays with thicker wires will work successfully on experiments with peak currents of 10 MA or more.

ACKNOWLEDGMENTS

The authors thank Todd Blanchard and Harry Wilhelm for their work in support of the experiments and Sergey Lebedev for his insight into the inverse skin effect in a moving plasma column. This work was funded by NSF and NNSA under Grant No. PHY2108050, by the EAGER Grant No. PHY2213898, and supported by the MathWorks fellowship. Simulations were performed on the Engaging cluster funded by DE-FG02-91-ER54109.

AUTHOR DECLARATIONS

Conflict of Interest

The authors have no conflicts to disclose.

Author Contributions

Rishabh Datta: conceptualization (equal); formal analysis (lead); investigation (equal); methodology (equal); software (equal); visualization (lead); writing—original draft (lead); and writing—review and editing (lead). **Jay Angel:** investigation (equal). **John Greenly:** conceptualization (equal) and investigation (equal). **Simon N. Bland:** writing—review and editing (equal). **Jeremy P. Chittenden:** software (equal) and writing—review and editing (equal). **Eric Sander Lavine:** investigation (equal). **William Potter:** investigation (equal). **Dylan Robinson:** formal analysis (supporting). **Thomas W. O. Varnish:** formal analysis (supporting). **Emily Wong:** formal analysis (supporting). **David Hammer:** resources (equal) and writing—review and editing (equal). **Bruce Kusse:** resources (equal) and writing—review and editing (equal). **Jack D. Hare:** conceptualization (equal); investigation (equal); project administration (equal); supervision (equal); and writing—review and editing (equal).

DATA AVAILABILITY

The data that support the findings of this study are available from the corresponding author upon reasonable request.

REFERENCES

[1]A. J. Harvey-Thompson, S. V. Lebedev, S. N. Bland, J. P. Chittenden, G. N. Hall, A. Marocchino, F. Suzuki-Vidal, S. C. Bott, J. B. Palmer, and C. Ning, "Quantitative analysis of plasma ablation using inverse wire array Z pinches," Phys. Plasmas **16**, 022701 (2009).

[2]S. Lebedev, L. Suttle, G. Swadling, M. Bennett, S. Bland, G. Burdiak, D. Burgess, J. Chittenden, A. Ciardi, A. Clemens *et al.*, "The formation of reverse shocks in magnetized high energy density supersonic plasma flows," Phys. Plasmas **21**, 056305 (2014).

[3]G. Burdiak, S. Lebedev, S. Bland, T. Clayson, J. Hare, L. Suttle, F. Suzuki-Vidal, D. Garcia, J. Chittenden, S. Bott-Suzuki *et al.*, "The structure of bow shocks formed by the interaction of pulsed-power driven magnetised plasma flows with conducting obstacles," Phys. Plasmas **24**, 072713 (2017).

[4]D. R. Russell, G. C. Burdiak, J. J. Carroll-Nellenback, J. Halliday, J. Hare, S. Merlini, L. G. Suttle, V. Valenzuela-Villaseca, S. Eardley, J. A. Fullalove *et al.*, "Perpendicular subcritical shock structure in a collisional plasma experiment," Phys. Rev. Lett. **129**, 225001 (2022).

[5]R. Datta, D. R. Russell, I. Tang, T. Clayson, L. G. Suttle, J. P. Chittenden, S. V. Lebedev, and J. D. Hare, "The structure of 3-D collisional magnetized bow shocks in pulsed-power-driven plasma flows," J. Plasma Phys. **88**, 905880604 (2022).

[6]L. G. Suttle, G. C. Burdiak, C. L. Cheung, T. Clayson, J. W. Halliday, J. D. Hare, S. Rusli, D. Russell, E. Tubman, A. Ciardi *et al.*, "Interactions of magnetized plasma flows in pulsed-power driven experiments," Plasma Phys. Controlled Fusion **62**, 014020 (2019).

[7]J. Hare, L. Suttle, S. Lebedev, N. Loureiro, A. Ciardi, J. Chittenden, T. Clayson, S. Eardley, C. Garcia, J. Halliday *et al.*, "An experimental platform for pulsed-power driven magnetic reconnection," Phys. Plasmas **25**, 055703 (2018).

[8]L. Suttle, J. Hare, S. Lebedev, A. Ciardi, N. Loureiro, G. Burdiak, J. Chittenden, T. Clayson, J. Halliday, N. Niasse *et al.*, "Ion heating and magnetic flux pile-up in a magnetic reconnection experiment with super-Alfvénic plasma inflows," Phys. Plasmas **25**, 042108 (2018).

[9]S. Lebedev, F. Beg, S. Bland, J. Chittenden, A. Dangor, and M. Haines, "Snowplow-like behavior in the implosion phase of wire array Z pinches," Phys. Plasmas **9**, 2293–2301 (2002).

[10]D. Sinars, M. Sweeney, C. Alexander, D. Ampleford, T. Ao, J. Apruzese, C. Aragon, D. Armstrong, K. Austin, T. Awe *et al.*, "Review of pulsed power-driven high energy density physics research on Z at Sandia," Phys. Plasmas **27**, 070501 (2020).

[11]M. R. Gomez, S. B. Hansen, K. J. Peterson, D. Bliss, A. Carlson, D. Lamppa, D. Schroen, and G. Rochau, "Magnetic field measurements via visible spectroscopy on the Z machine," Rev. Sci. Instrum. **85**, 11E609 (2014).

[12]T. Shelkovenko, S. Pikuz, J. Douglass, I. Blesener, J. Greenly, R. McBride, D. Hammer, and B. Kusse, "Wire core and coronal plasma expansion in wire-array Z pinches with small numbers of wires," Phys. Plasmas **14**, 102702 (2007).

[13]S. Lebedev, A. Frank, and D. Ryutov, "Exploring astrophysics-relevant magnetohydrodynamics with pulsed-power laboratory facilities," Rev. Mod. Phys. **91**, 025002 (2019).

[14]S. Bland, S. Lebedev, J. Chittenden, D. Ampleford, and G. Tang, "Use of linear wire array Z pinches to examine plasma dynamics in high magnetic fields," Phys. Plasmas **11**, 4911–4921 (2004).

[15]J. Hare, R. Datta, J. Chittenden, A. Crilly, W. Fox, J. Halliday, C. Jennings, H. Ji, C. Kuranz, S. Lebedev *et al.*, "Simulations of the MARZ (magnetically ablated reconnection on Z) platform," in *64th Annual Meeting of the APS Division of Plasma Physics*, Spokane, WA, 17–21 October 2022 (APS, 2022).

[16]R. Datta, J. Chittenden, A. Crilly, W. Fox, J. Halliday, C. Jennings, H. Ji, C. Kuranz, R. Melean, S. Lebedev *et al.*, "Plasma flows from dual exploding wire arrays for the MARZ campaign on Z," in *64th Annual Meeting of the APS Division of Plasma Physics*, Spokane, WA, 17–21 October 2022 (APS, 2022).

[17]V. L. Kantsyrev, L. I. Rudakov, A. S. Safronova, D. A. Fedin, V. V. Ivanov, A. L. Velikovich, A. A. Esaulov, A. Chuvatin, K. Williamson, N. D. Ouart *et al.*,

"Planar wire array as powerful radiation source," IEEE Trans. Plasma Sci. **34**, 2295–2302 (2006).
[18] A. Esaulov, A. Velikovich, V. Kantsyrev, T. Mehlhorn, and M. Cuneo, "Wire dynamics model of the implosion of nested and planar wire arrays," Phys. Plasmas **13**, 120701 (2006).
[19] V. Kantsyrev, L. Rudakov, A. Safronova, A. Velikovich, V. Ivanov, C. Coverdale, B. Jones, P. LePell, D. Ampleford, C. Deeney *et al.*, "Properties of a planar wire arrays Z-pinch source and comparisons with cylindrical arrays," High Energy Density Phys. **3**, 136–142 (2007).
[20] V. Kantsyrev, L. Rudakov, A. Safronova, A. Esaulov, A. Chuvatin, C. Coverdale, C. Deeney, K. Williamson, M. Yilmaz, I. Shrestha *et al.*, "Double planar wire array as a compact plasma radiation source," Phys. Plasmas **15**, 030704 (2008).
[21] B. Jones, D. Ampleford, R. Vesey, M. E. Cuneo, C. Coverdale, E. Waisman, M. Jones, W. Fowler, W. Stygar, J. Serrano *et al.*, "Planar wire-array Z-pinch implosion dynamics and x-ray scaling at multiple-MA drive currents for a compact multisource hohlraum configuration," Phys. Rev. Lett. **104**, 125001 (2010).
[22] J. Chittenden, S. Lebedev, B. Oliver, E. Yu, and M. Cuneo, "Equilibrium flow structures and scaling of implosion trajectories in wire array Z pinches," Phys. Plasmas **11**, 1118–1127 (2004).
[23] B. Jones, C. Deeney, J. L. McKenney, C. J. Garasi, T. A. Mehlhorn, A. C. Robinson, S. E. Wunsch, S. N. Bland, S. V. Lebedev, J. P. Chittenden *et al.*, "Study of three-dimensional structure in wire-array Z pinches by controlled seeding of axial modulations in wire radius," Phys. Rev. Lett. **95**, 225001 (2005).
[24] P. Knapp, J. Greenly, P.-A. Gourdain, C. Hoyt, M. Martin, S. Pikuz, C. Seyler, T. Shelkovenko, and D. Hammer, "Growth and saturation of the axial instability in low wire number wire array Z pinches," Phys. Plasmas **17**, 012704 (2010).
[25] A. L. Velikovich, I. V. Sokolov, and A. A. Esaulov, "Perfectly conducting incompressible fluid model of a wire array implosion," Phys. Plasmas **9**, 1366–1380 (2002).
[26] S. V. Lebedev, D. J. Ampleford, S. N. Bland, S. C. Bott, J. P. Chittenden, J. Goyer, C. Jennings, M. G. Haines, G. N. Hall, D. A. Hammer, J. B. Palmer, S. A. Pikuz, T. A. Shelkovenko, and T. Christoudias, "Physics of wire array Z-pinch implosions: Experiments at Imperial College," Plasma Phys. Controlled Fusion **47**, A91 (2005).
[27] J. Greenly, J. Douglas, D. Hammer, B. Kusse, S. Glidden, and H. Sanders, "A 1 MA, variable risetime pulse generator for high energy density plasma research," Rev. Sci. Instrum. **79**, 073501 (2008).
[28] J. Douglass, S. Pikuz, T. Shelkovenko, D. Hammer, S. Bland, S. Bott, and R. McBride, "Structure of the dense cores and ablation plasmas in the initiation phase of tungsten wire-array Z pinches," Phys. Plasmas **14**, 012704 (2007).
[29] E. Lavine, S. Rocco, W. Potter, J. Angel, E. Freeman, J. Banasek, J. Lawson, J. Greenly, H. Wilhelm, D. Hammer *et al.*, "Measurements of the imploding plasma sheath in triple-nozzle gas-puff Z pinches," Phys. Plasmas **29**, 062702 (2022).
[30] I. H. Hutchinson, "Principles of plasma diagnostics," in *Plasma Physics and Controlled Fusion,* 2nd ed. (Cambridge University Press, 2002), Vol. 44, p. 2603.
[31] G. F. Swadling, S. V. Lebedev, N. Niasse, J. P. Chittenden, G. N. Hall, F. Suzuki-Vidal, G. Burdiak, A. J. Harvey-Thompson, S. N. Bland, P. D. Grouchy, E. Khoory, L. Pickworth, J. Skidmore, and L. Suttle, "Oblique shock structures formed during the ablation phase of aluminium wire array Z-pinches," Phys. Plasmas **20**, 022705 (2013).
[32] J. D. Hare, J. MacDonald, S. N. Bland, J. Dranczewski, J. W. Halliday, S. V. Lebedev, L. G. Suttle, E. R. Tubman, and W. Rozmus, "Two-colour interferometry and Thomson scattering measurements of a plasma gun," Plasma Phys. Controlled Fusion **61**, 085012 (2019).
[33] R. Datta, D. Russell, I. Tang, T. Clayson, L. Suttle, J. Chittenden, S. Lebedev, and J. Hare, "Time-resolved velocity and ion sound speed measurements from simultaneous bow shock imaging and inductive probe measurements," Rev. Sci. Instrum. **93**, 103530 (2022).
[34] S. V. Lebedev, R. Aliaga-Rossel, S. N. Bland, J. P. Chittenden, A. E. Dangor, M. G. Haines, and I. H. Mitchell, "The dynamics of wire array Z-pinch implosions," Phys. Plasmas **6**, 2016–2022 (1999).
[35] S. Pikuz, T. Shelkovenko, A. Mingaleev, D. Hammer, and H. Neves, "Density measurements in exploding wire-initiated plasmas using tungsten wires," Phys. Plasmas **6**, 4272–4283 (1999).
[36] J. Wu, L. Wang, J. Han, M. Li, L. Sheng, Y. Li, M. Zhang, N. Guo, T. Lei, A. Qiu *et al.*, "X-pinch radiography for the radiation suppressed tungsten and aluminum planar wire array," Phys. Plasmas **19**, 022702 (2012).
[37] K. Muraoka and M. Maeda, *Laser-Aided Diagnostics of Plasmas and Gases* (CRC Press, 2016).
[38] A. Ciardi, S. V. Lebedev, A. Frank, E. G. Blackman, J. P. Chittenden, C. Jennings, D. J. Ampleford, S. Bland, S. C. Bott, J. Rapley *et al.*, "The evolution of magnetic tower jets in the laboratory," Phys. Plasmas **14**, 056501 (2007).
[39] M. G. Haines, "The inverse skin effect," Proc. Phys. Soc. **74**, 576 (1959).
[40] L. Suttle, J. Hare, J. Halliday, S. Merlini, D. Russell, E. Tubman, V. Valenzuela-Villaseca, W. Rozmus, C. Bruulsema, and S. Lebedev, "Collective optical Thomson scattering in pulsed-power driven high energy density physics experiments," Rev. Sci. Instrum. **92**, 033542 (2021).